

Cite this: DOI: 10.1039/xxxxxxxxxx

Desorption dynamics of RbHe exciplexes off He nanodroplets induced by spin relaxation[†]

François Coppens,^a Johannes von Vangerow,^b Manuel Barranco,^{a,c} Nadine Halberstadt,^a Frank Stienkemeier,^b Martí Piç, and Marcel Mudrich,^d

Received Date
Accepted Date

DOI: 10.1039/xxxxxxxxxx

www.rsc.org/journalname

Doped He nanodroplets are ideal model systems to study the dynamics of elementary photophysical processes of heterogeneous nanosystems. Here we present a combined experimental and theoretical investigation of the formation of free RbHe exciplex molecules from laser-excited Rb-doped He nanodroplets. Upon excitation of a droplet-bound Rb atom to the $5p_{3/2}(\Pi_{3/2})$ -state, a stable RbHe exciplex forms within about 50 ps. Only due to $\Pi_{3/2} \rightarrow \Pi_{1/2}$ spin-relaxation does the RbHe exciplex detach from the He droplet surface within about 700 ps, given by the spin-relaxation time and the coupling of spin and translational degrees of freedom.

1 Introduction

Understanding the photochemistry of condensed phase systems and surfaces is essential in many research areas, such as atmospheric sciences¹ and photocatalysis². However, complex diabatic couplings of electronic and motional degrees of freedom of various subunits of the system often present a major challenge. Moreover, the heterogeneity of multi-component solid or liquid systems and experimental difficulties in precisely preparing the sample and reproducing measurements tend to make it hard to unravel specific elementary reactions. In this respect, He nanodroplets doped with single atoms or well-defined complexes are ideal model systems for studying photodynamical processes in the condensed phase, both experimentally and theoretically. Due to their ultralow temperature (0.37 K) and their quantum fluid nature, He nanodroplets have a homogeneous density distribution and dopant particles aggregate into cold clusters mostly inside the droplets^{3,4}. Only alkali metal atoms and small clusters are attached to He droplets in loosely bound dimple-like states at the droplet surface^{5–12}.

While He nanodroplets are extremely inert and weakly-perturbing matrices for spectroscopy of embedded atoms and molecules in their electronic ground state, a rich photochemical

dynamics is initiated upon electronic excitation or ionization^{13,14}, involving electronic relaxation^{15–18}, the ejection of the dopant out of the droplet^{19–26}, chemical reactions within the dopant complex^{27–29}, and even among the dopant and the surrounding He^{20,30–39}.

As a general trend, electronically excited dopant atoms and small molecules tend to be ejected out of He droplets either as bare particles or with a few He atoms attached to them^{15,40–42}. In particular, all atomic alkali species promptly desorb off the droplet surface, the only exceptions being Rb and Cs atoms in their lowest excited states^{43,44}. The dynamics of the desorption process has recently been studied at an increasing level of detail^{16,21,23,45}, including time-resolved experiments and simulations^{24,26}. The focus was on the competing processes of desorption of the dopant induced by laser excitation, and the dopant falling back into the He droplet upon photoionization. The latter occurred at short pump-probe delay times when the distance between the photoion and the droplet was short enough for ion-He attraction to be effective.

The purpose of this work is to extend our joint experimental and theoretical study of the photodynamics of Rb-doped He nanodroplets to RbHe exciplexes^{23,26}. The simultaneous effect of pair-wise Rb-He attraction and repulsion of Rb from the He droplet as a whole results in an intricate dynamics, and interpretations have remained somewhat ambiguous with respect to the exciplex formation mechanism and time scale, as well as the origin of free exciplexes detached from the He droplets^{16,26,30,33,34}. In particular the role of relaxation of internal degrees of freedom of the RbHe exciplex in the desorption process has not been explicitly addressed^{46,47}. Here, we discuss in detail the interplay of the RbHe formation dynamics, the RbHe desorption off the He droplet surface, and the fall-back of $[\text{RbHe}]^+$ created by pho-

^a Laboratoire des Collisions, Agrégats, Réactivité, IRSAMC, UMR 5589, CNRS et Université Paul Sabatier-Toulouse 3, 118 route de Narbonne, F-31062 Toulouse Cedex 09, France

^b Physikalisches Institut, Universität Freiburg, Hermann-Herder-Str. 3, 79104 Freiburg, Germany

^c Institute of Nanoscience and Nanotechnology (IN2UB), Universitat de Barcelona, Diagonal 645, 08028 Barcelona, Spain

^d Department of Physics and Astronomy, Aarhus University, Ny Munkegade 120, Aarhus 8000 C, Denmark

* E-mail: mudrich@phys.au.dk

to ionization in femtosecond pump-probe experiments^{24,26,31}. We find that electronic spin-relaxation is the main process driving the desorption of RbHe off the He droplet.

2 Methods

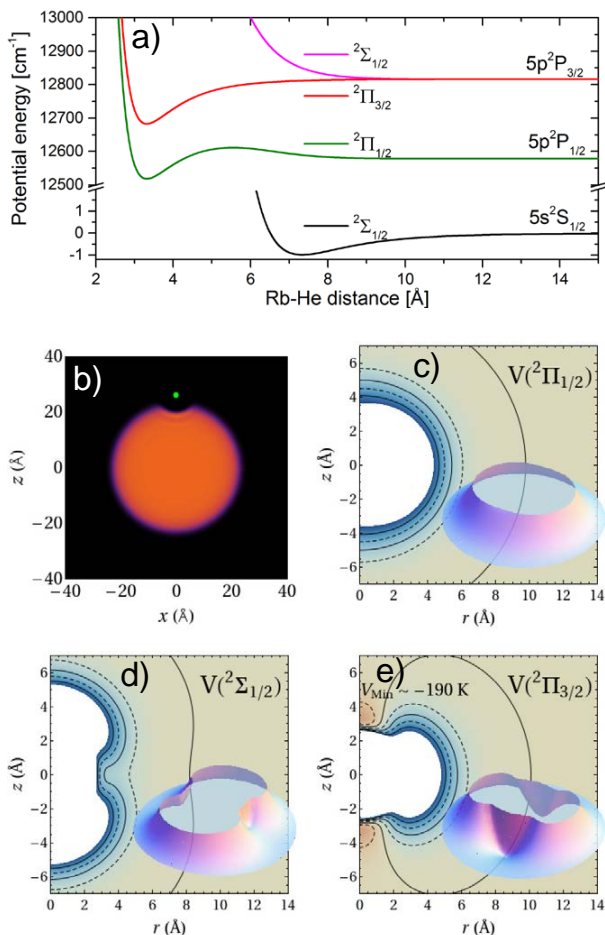


Fig. 1 (Color online) a) Rb-He pair potentials used in this work^{48,53}. The potentials correlating to the Rb excited $5p^2P$ -state are split due to spin-orbit. b) Equilibrium dimple configuration of Rb in the groundstate (represented by a green dot). Panels c)-e) display the two-dimensional Rb-He potential surfaces corresponding to this configuration. Regions where the potentials are attractive (repulsive) are represented in brown (blue). The outermost equidensity line corresponds to zero potential. The $5p^2\Sigma_{1/2}$ and $5p^2\Pi_{1/2}$ potentials have a shallow attractive minimum of about 1 K depth at a distance of ~ 10 Å not represented in the figure.

2.1 Theoretical approach

During the last decade, the density functional theory (DFT) approach has emerged as an accurate and flexible tool to describe the statics and dynamics of doped helium droplets. The DFT activity carried out in this field has been summarized in two reviews^{7,14}. In the following we give the basic details how the method has been applied to the present problem, and refer the reader to Refs.^{14,22} for the details.

In this work, we describe the interaction of a Rb atom with a He droplet composed of $N = 1000$ He atoms. Due to its large mass,

Rb is treated as an external field in the statics, and as a classical particle in the dynamics. The impurity-droplet interaction is described in a pairwise approximation, and the groundstate of the droplet-impurity system is found by solving the Euler-Lagrange equation

$$\left\{ -\frac{\hbar^2}{2m} \nabla^2 + \frac{\delta \mathcal{E}_c}{\delta \rho} + V_X(|\mathbf{r} - \mathbf{r}_I|) \right\} \Psi_0(\mathbf{r}) = \mu \Psi_0(\mathbf{r}), \quad (1)$$

where $\Psi_0(\mathbf{r}) = \sqrt{\rho(\mathbf{r})}$ is the He effective wave function, with $\rho(\mathbf{r})$ being the atom density; μ is the He chemical potential, and V_X is the Rb-He pair potential⁴⁸. The correlation energy density functional \mathcal{E}_c has been taken from Ref.⁴⁹. The results presented in this work are obtained using the 4He-DFT BCN-TLS computing package⁵⁰. We work in cartesian coordinates using a space-step of 0.4 Å.

Once the droplet-equilibrium configuration shown in Fig. 1 b) is determined, the $5p \leftarrow 5s$ absorption spectrum is obtained using the DF sampling method⁵¹. To this end, the diatomic-in-molecule model is used for the droplet-Rb interaction in the excited $5p^2P$ state⁵². The $5p\Sigma$ and $5p\Pi$ Rb*-He pair potentials, shown in Fig. 1 a), are taken from Refs.^{48,53}. The resulting simulated absorption dipole spectrum of the RbHe₁₀₀₀ complex, shown in Fig. 6 of Ref.¹⁴, is in good agreement with the experiment and previous calculations^{31,54}.

Figs. 1 c)-e) show the direction-dependent potentials (spin-orbit term included) which, within the diatomic-in-molecule approach, enter the dynamics simulations of Rb in the $5p^2P$ -correlated states. In the course of the time evolution of the system, the He atoms have a natural tendency to adapt to these potential surfaces, either going away if the potential is mostly repulsive as in the $\Sigma_{1/2}$ -state [Fig. 1 d)], or to evolve to a bound RbHe exciplex configurations in the $\Pi_{3/2}$ -state [e)] featuring local minima at $(r=0, z=\pm 3.5$ Å). In the $\Pi_{1/2}$ -state near the D1-line transition [c)], one may also expect the formation of RbHe exciplexes given the potential minimum in the RbHe pair potential around 3.2 Å [Fig. 1 a)]. However, RbHe formation is hampered by a potential barrier which cannot be overcome at the low temperature of the He droplet^{31,55}.

2.2 Experimental setup

The setup used for the present experiments has been described previously^{23,24}. Briefly, a beam of He droplets with an average diameter of 10 nm is produced by continuously expanding pressurized He (50 bar) out of a cold nozzle (diameter 5 μ m, temperature 17 K). The He droplets are doped with one Rb atom on average by pickup of Rb atoms inside a heated vapor cell (length 1 cm, temperature 85°C).

An amplified Ti:Sa laser system generates pulses of 100 fs duration at a repetition rate of 5 kHz. The center wavelength is tunable in the near infrared (NIR) region. The FWHM of the spectral laser profile is 140 cm^{-1} . Light in the visible range (VIS) is generated by frequency doubling. The pulses are split and separated in time in a Mach-Zehnder type interferometer. The droplet perturbed Rb $5p$ states are probed by a two-color NIR+VIS pump-probe resonant photoionization scheme. The NIR

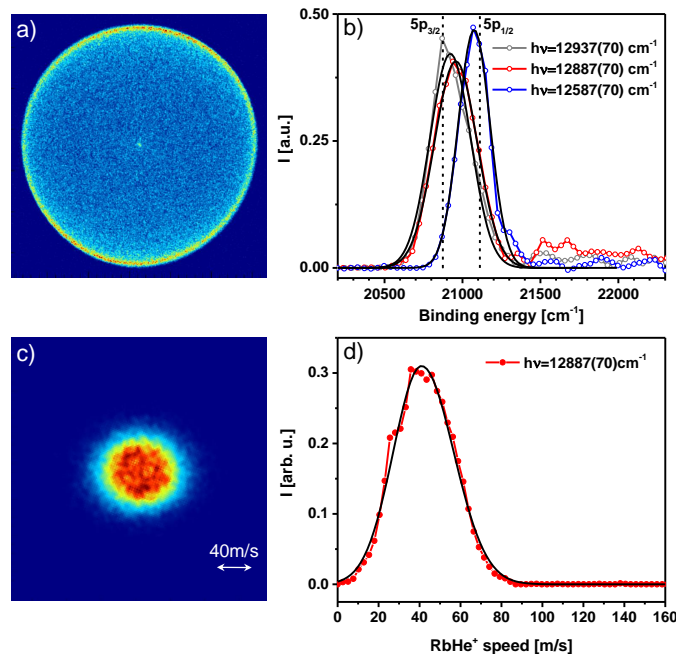


Fig. 2 Raw velocity-map images of photoelectrons a) and of RbHe^+ photoions c) recorded at $\lambda = 776$ nm (12887 cm^{-1}) for a long pump-probe delay time of 2 ns. b) Electron binding energies inferred from the image in a) and from images recorded at $\lambda = 773$ nm (12937 cm^{-1}) and at $\lambda = 794$ nm (12587 cm^{-1}). d) RbHe^+ photoion speed distribution inferred from c).

pulses are strongly attenuated to avoid the excitation of higher lying states by multi-photon processes. Polarizations of the two laser pulses are parallel to one another and parallel to the detector surface.

Photoions and photoelectrons are detected by a velocity-map imaging (VMI) spectrometer operated in centroid detection mode^{16,23,56,57}. Mass-selected ion VMIs are recorded for varying pump-probe delay times and are inverse Abel-transformed^{58,59}. Both Rb^+ ion images and electron images contain background contributions stemming from resonant ionization of free Rb atoms effusing out of the doping cell. In order to efficiently subtract these contributions, background images are recorded at each pump-probe delay using a chopper running at a frequency of 15 Hz. Acquired background and signal+background images are inverse Abel transformed. The resulting spectra are normalized to the number of counts and subtracted from each other exploiting the additivity of the inverse Abel transformation⁶⁰.

3 Time-resolved imaging spectroscopy

Typical experimental total electron and RbHe^+ ion VMIs recorded at a center wavelength of the pump laser pulse $\lambda = 776$ nm and a pump-probe delay of 2 ns are shown in Fig. 2 a) and c), respectively. In these VMIs, the laser polarization is oriented along the y-axis. The corresponding electron energy distribution and ion speed distribution inferred from these images are presented in Fig. 2 b) and d), respectively. In addition, Fig. 2 b) contains photoelectron spectra measured at $\lambda = 773$ and 794 nm. Note that the photoelectron spectra in Fig. 2 b) are rescaled in terms of electron

binding energies $E_b = h\nu_2 - T_e$, where $h\nu_2 = 2hc/\lambda$ denotes the photon energy of the ionizing laser pulse and T_e is the measured electron kinetic energy. The dashed vertical lines represent E_b of the free atomic $5p_{1/2}$ and $5p_{3/2}$ -states.

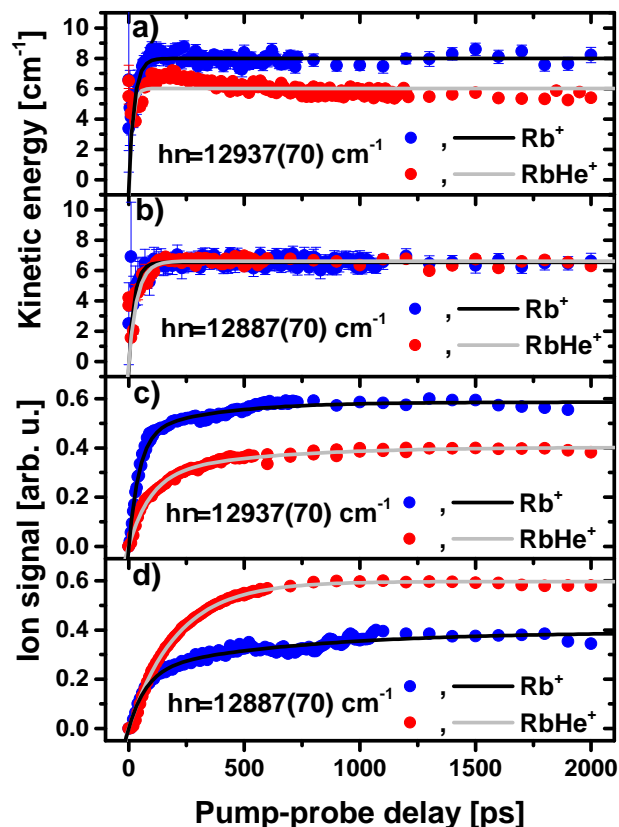


Fig. 3 Rb^+ and RbHe^+ ion kinetic energies [a) and b)] and signal yields [c) and d)] recorded at laser wavelengths $\lambda = 773$ nm [12937 cm^{-1} , a) and c)] and $\lambda = 776$ nm [12887 cm^{-1} , b) and d)].

3.1 Photoion imaging

The RbHe^+ ion distribution [Fig. 2 c)] is a round spot with a flat intensity distribution and a slight elongation in x-direction (perpendicular to the laser polarization). The corresponding speed distribution is broad and nearly symmetric. The red line depicts a skewed Gaussian distribution fitted to the data⁶¹. This fit is applied repeatedly to each speed distribution measured at various pump-probe delays in order to trace the evolution of the most probable kinetic energy, see Fig. 3 a) and b). The yields of ions, shown in Fig. 3 c) and d), are obtained by summing over ion counts contained in each image. Blue and red symbols show the results for Rb^+ and RbHe^+ ions, respectively. Both kinetic energies and ion yields monotonously increase within 100-500 ps, with a slight overshoot at $\lambda = 773$ nm [Fig. 3 a)]. This dynamics results from the competing processes of desorption of the excited neutral Rb and RbHe species, and the falling back of the Rb^+ and RbHe^+ photoions into the He droplet due to attractive Rb^+ -He interactions, as discussed in Refs.^{24,26}. By comparing the experimental data with TD-DFT dynamics simulations, we concluded that the 5p-correlated states of Rb and RbHe desorb

off He droplets not purely impulsively, but in a more complex evaporation-like process²⁶. The overshoot of speeds in Fig. 3 a) is likely due to weak long-range attractive forces acting between the desorbing Rb and RbHe and the He droplet surface, which slightly slow down the relative motion in the later stage of desorption.

The data in Fig. 3 a) are measured at $\lambda = 773$ nm (12937 cm^{-1}), which corresponds to the excitation of the RbHe complex into the $5p\Sigma_{1/2}$ -state, with some contribution of the $5p\Pi_{3/2}$ -state due to overlapping absorption bands and due to the broad spectral width of the laser and ^{6,31,62}. The $5p\Sigma_{1/2}$ -state is the most repulsive one out of the three states studied here. Accordingly, the asymptotic most probable speed of Rb^+ reached at long delays is comparatively high, $\hat{v} = 85\text{ m/s}$, corresponding to a kinetic energy of 8 cm^{-1} , whereas for RbHe^+ we find $\hat{v} = 40\text{ m/s}$ (5.8 cm^{-1}). Since the diatomic $5p\Sigma_{1/2}$ RbHe potential is purely repulsive [Fig. 1 a)], this component of the excited population yields neat desorbed Rb atoms. Accordingly, the yield of detected Rb^+ ions exceeds that of RbHe^+ ions by about a factor 1.5.

At $\lambda = 776$ nm (12887 cm^{-1}), a higher contribution of the $5p\Pi_{3/2}$ -state is excited, which efficiently forms RbHe exciplexes³¹. Thus, the yield of RbHe^+ ions is higher than that of Rb^+ by a factor 1.5. The Rb^+ and RbHe^+ asymptotic most probable speed is 42 m/s (6.3 cm^{-1}), close to that of RbHe^+ at $\lambda = 773$ nm. At $\lambda = 794$ nm (12595 cm^{-1} , $5p\Pi_{1/2}$ -state of the Rb-He droplet complex, not shown), no RbHe^+ ions are detected. Therefore we have recorded only Rb^+ ion images at that wavelength²⁶. Here, the Rb^+ asymptotic most probable speed is lowest, 38 m/s (5.1 cm^{-1}), because dopant-He repulsion is weakest.

The transient kinetic energies measured at all laser wavelengths rise within a delay time of about 500 ps. The characteristic energy rise time (to half value), τ_d , and the asymptotic ion kinetic energy E^I , are determined by fitting the data with an exponential function

$$E^I(t) = E^I \cdot (1 - \exp[-\ln 2 \cdot t / \tau_d]). \quad (2)$$

The resulting fit parameters are summarized in table 1.

The ion yields increase with pump-probe delay slightly more slowly than the ion kinetic energies, where the Rb^+ ion signal rises faster than the RbHe^+ ion signal at short delays. The initial fast rise of the Rb^+ ion yield flattens out at delays around 100 ps and continues to rise slightly up to about 2 ns. The RbHe^+ ion yields show a similar initial fast rise followed by a more pronounced slow increase that levels off somewhat earlier. For fitting the Rb^+ and RbHe^+ ion yield data we use a biexponential function,

$$I(t) = A \cdot (1 - \exp[-\ln 2 \cdot t / \tau]) + A^* \cdot (1 - \exp[-\ln 2 \cdot t / \tau^*]), \quad (3)$$

where (A, τ) and (A^*, τ^*) parametrize the fast and the slow signal rise, respectively.

While neither the Rb^+ and RbHe^+ asymptotic energies E^I , nor the energy rise times τ_d depend much on λ , the rise times of ion yields of RbHe^+ , τ , clearly decrease monotonically with decreasing λ (increasing photon energy) by a factor 6, ranging from

186 ps at $\lambda = 780$ nm to 33 ps at $\lambda = 773$ nm.

The trend that the dynamics proceeds faster with decreasing λ (increasing photon energy) is due to the increasingly repulsive dopant-He interaction and agrees with our previous findings^{24,26}. However, the observation that the ion yields rise more slowly than the ion kinetic energies cannot be understood with the concept of impulsive desorption and fall-back. In that model, ion kinetic energies should be affected by ion-He attraction up to long delay times exceeding the fall-back time. Note that in previous experiments on the Rb $5p$ -state, where desorption proceeded impulsively, ion energies indeed increased more slowly than ion yields²⁶. Therefore we take our current finding ($\tau, \tau^* > \tau_d$) as a further indication for a non-impulsive, evaporation-like desorption dynamics.

Furthermore, from our analysis of the VMIs we obtain information about the anisotropy of the ion angular distribution, characterized by the parameter β ¹⁶. For long delay times we find $\beta = -0.36(1)$ when exciting mainly the $\Pi_{3/2}$ -state at $\lambda = 776$ nm. At $\lambda = 773$ nm (mainly $\Sigma_{1/2}$ -excitation), the anisotropy becomes slightly positive, $\beta = 0.13(1)$. The corresponding values for the Rb^+ ion distributions are $\beta = -0.16(1)$ and $\beta = 0.17(1)$, respectively. While the signs of the β -values are in agreement with the symmetries of coupled states (ideal perpendicular $\Sigma \rightarrow \Pi$ -transition in a diatomic implies $\beta = -1$, parallel $\Sigma \rightarrow \Sigma$ -transition implies $\beta = 2$), the absolute values are much less. On the one hand, this is due to the mixture of excited $\Sigma_{1/2}$ and $\Pi_{3/2}$ -states. On the other hand, the desorption process is significantly more complex than direct dissociation of a diatomic molecule. We recall that the β -values came much closer to the ideal values in the case of excitation of Rb to the high-lying $6p$ -correlated states, where desorption proceeded more impulsively^{16,23,26}. The larger absolute value of β measured at $\lambda = 776$ nm for $[\text{RbHe}]^+$ likely reflects the fact that RbHe exciplexes are formed only from the $\Pi_{3/2}$ -part of the excited state.

We mention that in earlier pump-probe experiments, significantly differing Rb^+ and $[\text{RbHe}]^+$ ion yield curves were measured³³. However, in those experiments, near-infrared light emitted directly from a mode-locked titanium:sapphire laser was used at a pulse repetition rate of 80 MHz. Therefore, a large fraction of the ion signals actually stemmed from Rb and RbHe that were desorbed off the droplets by preceding pulse pairs. Thus, the observed pump-probe transients may have reflected the internal dynamics of free RbHe instead of the dynamics of the Rb-He droplet interaction. Besides, near-resonant two-photon excitation of higher lying states correlating to the Rb $5d$ -level were probably involved in the observed dynamics. This raises some doubts as to the conclusions of those previous experiments in terms of exciplex formation times^{26,33}. Further studies are needed to clarify this issue.

From the overall resemblance of the RbHe^+ and Rb^+ kinetic energy curves and ion yields in the present study one is tempted to conclude that RbHe exciplex formation is fast and desorption of RbHe off the He droplet surface proceeds essentially in the same way as for neat Rb atoms. However, the more pronounced biexponential rise of $[\text{RbHe}]^+$ ion yields, as well as complementary delay-dependent photoelectron measurements in combina-

λ [nm]	State	Ion	E^I [1/cm]	τ_d [ps]	A	τ [ps]	A^*	τ^* [ps]	β
773	$\Sigma_{1/2}/\Pi_{3/2}$	Rb ⁺	8.0(1)	17(1)	0.45(2)	32(1)	0.14(2)	234(33)	***
		RbHe ⁺	6.0(1)	10(2)	0.17(2)	41(6)	0.22(2)	178(17)	0.13(1)
776	$\Pi_{3/2}/\Sigma_{1/2}$	Rb ⁺	6.5(3)	17(1)	0.24(2)	53(5)	0.16(2)	490(104)	***
		RbHe ⁺	6.6(3)	26(1)	0.60(1)	143(2)	~ 0	-	-0.39(1)

Table 1 Time constants and energies inferred from the pump-probe measurements of mainly the $5p\Sigma_{1/2}$ and $5p\Pi_{3/2}$ -states, obtained from fits with equations (2 and 3), see Fig. 3.

tion with simulations presented in the following sections will show that the desorption dynamics of RbHe exciplexes is more complex than that of Rb atoms.

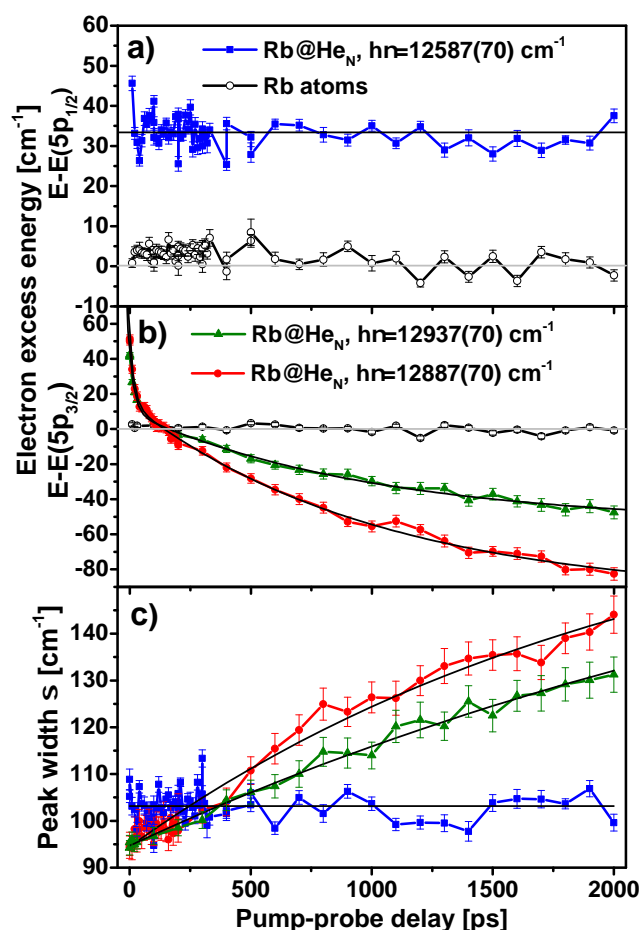


Fig. 4 Photoelectron energies as a function of pump-probe delay (filled circles) recorded at laser wavelengths $\lambda = 794$ nm ($5p\Pi_{1/2}$) (a), and $\lambda = 773$ nm ($5p\Sigma_{1/2}$) and $\lambda = 776$ nm ($5p\Pi_{3/2}$) (b). Open circles indicate the electron energies measured for atomic Rb background signal.

3.2 Photoelectron imaging

The photoelectron spectra recorded at the three characteristic laser wavelengths λ [Fig. 2 b)] exhibit pronounced peaks around the Rb $5p_{1/2}$ and $5p_{3/2}$ atomic binding energies, $E_{5p_{1/2}}$ and $E_{5p_{3/2}}$, respectively. Both the peak position and the peak width significantly vary with λ , as inferred from fits to the data with a Gaussian function, depicted as smooth lines. The resulting peak

positions relative to $E_{5p_{1/2}}$ and $E_{5p_{3/2}}$ are plotted in Fig. 4 a), b), respectively. Fig. 4 c) shows the peak widths σ . For reference, the open symbols represent the peak positions measured for the Rb atomic background. The scatter of data points around the literature value (grey horizontal line) indicates the level of precision of our measurements.

The excess energies for the $5p\Sigma_{1/2}$ and $5p\Pi_{3/2}$ -states, $E_b - E_{5p_{1/2}, 5p_{3/2}}$ [Fig. 4 b)] exhibit a fast decay (E_+^e , τ_+^e) above and a slow decay (E_-^e , τ_-^e) below $E_{5p_{3/2}}$ (horizontal line at $y = 0$). Therefore, these data are fitted with a biexponential decay function

$$E^e(t) = E_+^e \cdot \exp(-\ln 2 \cdot t / \tau_+^e) + E_-^e \cdot \exp(-\ln 2 \cdot t / \tau_-^e) + E_\infty^e. \quad (4)$$

Here, E_∞^e denotes the asymptotic energy value at long delay times. When exciting the $5p\Pi_{1/2}$ -state at $\lambda = 794$ nm, the transient droplet correlated peak position remains constant within the experimental scatter. Therefore, merely the mean value E_+^e is determined. The resulting energies and time constants are summarized in table 2. The increasing peak widths in the cases of $\lambda = 773$ and 776 nm are fitted by the simple exponential function given by Eq. 2.

The fact that the droplet-related photoelectron energy E_+^e for the $\Pi_{1/2}$ -state is constant but shifted with respect to the atomic value indicates that most of the Rb atoms remain attached to the droplet surface upon electronic excitation, in accordance with previous studies^{43,63}. Thus, the slowly rising Rb⁺-ion signal measured at that wavelength, indicative for excited Rb* desorption, reflects only a small fraction of Rb* atoms, most of which actually remain bound to the droplets. The measured up-shift of electron energy of $E_+^e = 33(2)$ cm⁻¹ is attributed to a lowering of the ionization threshold induced by the He environment. This value is in reasonable agreement with previous measurements, where the ionization threshold was found to be lowered by 50(10) cm⁻¹ at comparable conditions⁶³.

The similar dynamics of electron energies and ion yields for the $\Sigma_{1/2}$ and $\Pi_{3/2}$ -states – a biexponential evolution with a fast component (tens of ps) and a slow component (hundreds of ps) – we take as a confirmation that two distinct relaxation processes occur simultaneously. The fast process – prompt desorption of Rb* off the He droplet – is associated mainly with the $\Sigma_{1/2}$ -component of the excited state, whereas the $\Pi_{3/2}$ -component undergoes slow relaxation. The latter will be discussed in the following sections. Deviations of the time constants τ vs. τ_+^e , and τ^* vs. τ_-^e are mainly due to the different nature of the observables. Both ion yields and

λ [nm]	State	E_+^e [1/cm]	τ_+^e [ps]	E_-^e [1/cm]	τ_-^e [ps]	E_∞^e [1/cm]
773	$\Sigma_{1/2}/\Pi_{3/2}$	32(2)	15(2)	63(4)	683(130)	-53(5)
776	$\Pi_{3/2}/\Sigma_{1/2}$	36(2)	13(2)	110(4)	709(70)	-96(5)
794	$\Pi_{1/2}$	33(2)	-	-	-	-

Table 2 Time constants and energies inferred from the transient photoelectron energies (Fig. 4).

speeds are affected by the dynamics occurring after the probe-ionization, whereas electron spectra probe the spatial distribution (and electronic state) at the moment of ionization. In particular, ion signals provide information only about that fraction of ions that are eventually detached from the He droplets, whereas electron signals are measured for all photoionization events, including those where the ion falls back into the droplet; in this respect the electron spectra are the better probes of the full Rb^* dynamics, with the restriction that we cannot distinguish between the final products (Rb^* , $[\text{RbHe}]^*$, $[\text{Rb}^*\text{He}_N]$). For this, electron-ion coincidence detection would have to be applied, as e. g. in Ref. ⁶⁴.

We mention that at $\lambda = 776$ nm ($\Pi_{3/2}$ -state), an extended low intensity distribution is present in the spectrum [Fig. 4 b)] at higher electron binding energies $\geq 21,500$ cm^{-1} (lower electron kinetic energies). We attribute this component to elastic scattering of photoelectrons with He atoms as they propagate through the He droplet. Low-energy features in photoelectron spectra due to electron-He scattering have been observed previously, in particular when using one-photon ionization ^{64–67}. The fact that this feature is most pronounced for the $\Pi_{3/2}$ -excitation may be related to the more abundant formation of RbHe exciplexes which enhances the electron-He scattering probability.

4 TD-DFT dynamics simulation

Time-dependent density functional theory (TD-DFT) simulations are carried out as thoroughly described in Refs. ^{14,22}. The step width in time and space is 0.5 fs and 0.4 Å, respectively. Starting with the Rb -droplet equilibrium configuration, the dynamics is initiated by a “vertical DFT transition” into the excited state. This is realized by suddenly switching from the potential energy surface of the Rb -He droplet groundstate to that of the Rb^* -He excited state. The subsequent evolution of the system can be followed in real-time, as illustrated by the series of snapshots of the He density distribution (red area) and the position of the Rb atom (green and magenta dots) in Fig. 5. Here, excitation of the $5p\Pi_{3/2}$ -state at $t = 0$ is followed by relaxation to the $5p\Pi_{1/2}$ -state at $t = 60$ ps.

4.1 Direct ejection of bare Rb atoms from the $^2\Sigma_{1/2}$ and $^2\Pi_{1/2}$ -states

From these data we now infer the relevant quantities to compare with the experimental results, such as the kinetic energy of the Rb atom relative to the droplet, the occurrence of He density attached to Rb which we identify with the formation of an exciplex, and the transient interaction energy of the neutral and ionized Rb atom with the surrounding He. The latter is related to the kinetic energy of a photoelectron created in a time-delayed photoionization

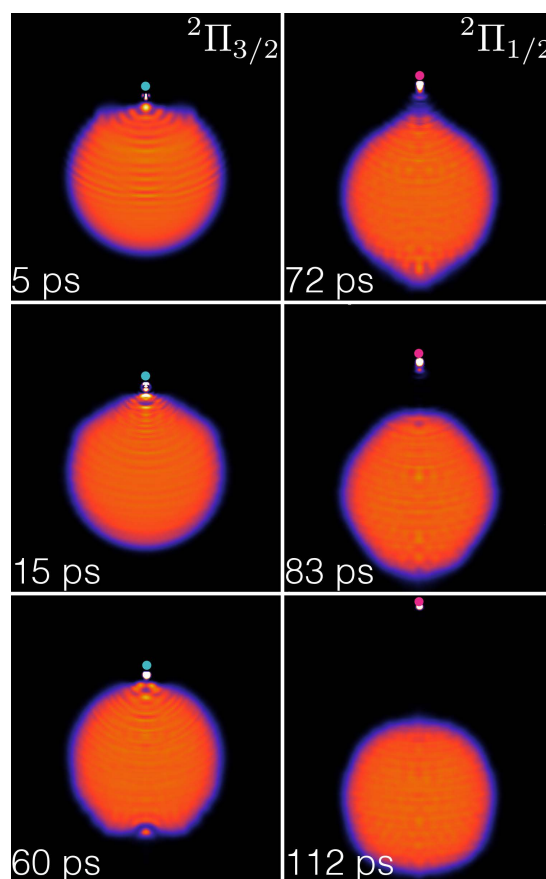


Fig. 5 Snapshots of the He density during the evolution of the $\text{Rb}^*\text{He}_{1000}$ complex for $\eta = 15\%$, $\tau = 60$ ps. The green dot represents the Rb^* atom excited into the $5p\Pi_{3/2}$ -state, and the magenta dot is the Rb^* atom after suddenly relaxing to the $5p\Pi_{1/2}$ -state.

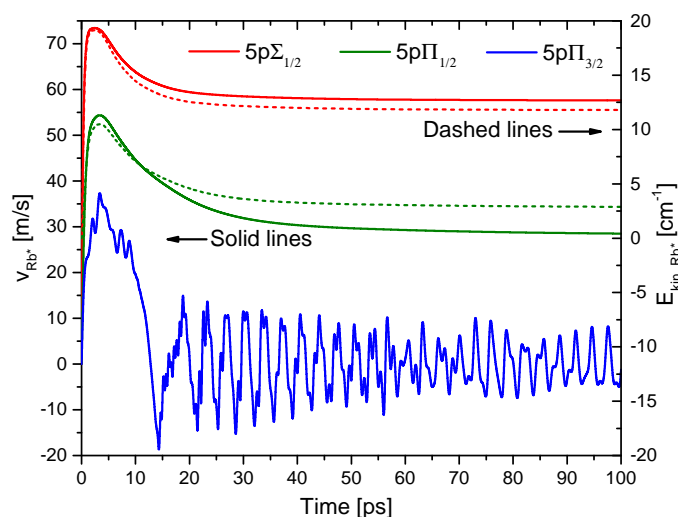


Fig. 6 (Color online) Velocity (dashed lines, right scale) and kinetic energy (solid lines, left scale) of the Rb atom excited to the 5p-state as a function of time. The kinetic energy of the $5p\Pi_{3/2}$ -state is not given as this state remains bound to the droplet.

process.

Fig. 6 collects our results for the dynamics of the Rb atom excited to the droplet-perturbed states correlating to the atomic 5p-state. For the $\Sigma_{1/2}$ and $\Pi_{1/2}$ -states, the velocities (dashed lines) and kinetic energy curves (solid lines) feature a rapid increase to reach a maximum at time $t = 2\text{--}5$ ps after excitation, followed by a drop due to long-range attractive forces acting on the desorbing Rb^* atom. The asymptotic values are reached for $t > 50$ ps. When exciting the $\Pi_{3/2}$ -state, the Rb^* -velocity features a damped oscillation around zero indicating that the Rb^* atom remains bound to the He droplet surface.

The following conclusions can be drawn from these results: (i) Rb excited to the $5p\Sigma_{1/2}$ -state detaches from the droplet reaching an asymptotic kinetic energy of 12 cm^{-1} ***. This value slightly deviates from the experimental one (8.0 cm^{-1}) due to contributions of $\Pi_{3/2}$ -excitation to the experimental signal. Despite of the shallow local minima in the corresponding Rb-He droplet potential surface [1 c)], no binding of He density to the departing Rb^* atom occurs. This finding is in accordance with experiments^{16,31,33}, where mostly free Rb atoms were detected following excitation at wavelengths $\lambda < 774\text{ nm}$.

(ii) Rb excited to the $5p\Pi_{1/2}$ -state also detaches from the He droplet, but the asymptotic kinetic energy is much lower, 2.8 cm^{-1} . This value again slightly deviates from the experimental one (5.1 cm^{-1}), but the trend that desorption of the less repulsive $\Pi_{1/2}$ -state yields a lower energy than for the $\Sigma_{1/2}$ -state is well reproduced. The potential well at short distance $\sim 3\text{ \AA}$ would in principle support a stable RbHe exciplex. However, at the low temperature of the He droplet, exciplex formation is hindered by a potential barrier located at $\sim 5\text{ \AA}$, between the well and the range where the $5p\Pi_{1/2}$ -state is populated by excitation from the $5s\Sigma_{1/2}$ -groundstate (7 \AA)^{30,31,55}.

We recall that in previous experiments using narrow-band ex-

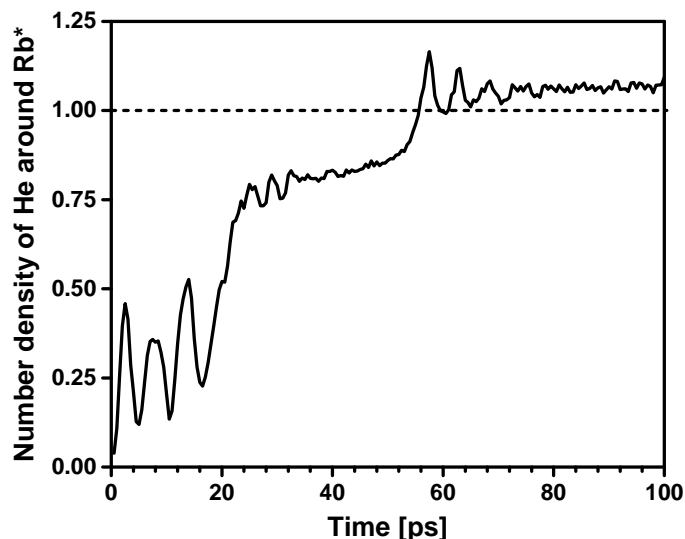


Fig. 7 (Color online) Simulated time evolution of the integrated He density within an inclusion volume of radius $r_{\text{incl}} = 5.7\text{ \AA}$ around the Rb atom excited to the $5p\Pi_{3/2}$ -state.

citation of the low energy edge of the $\Pi_{1/2}$ -resonance it was observed that Rb and Cs dopants remained attached to the He droplet surface⁴³. However, our simulations correspond to the excitation at the peak of the resonance, where free Rb atoms are also observed in the experiment. Thus, our simulations are not in conflict with the experimental findings. Note that Quantum Monte Carlo (QMC) calculations carried out for this state⁶⁸ yielded a weakly bound Rb^* in a shallow dimple. Had we carried out a *static* DFT relaxation, we would also have found a bound structure, due to the shallow minimum on the Rb-He droplet potential surface. However, in the dynamical TD-DFT simulation this minimum is too shallow to retain the departing Rb^* atom.

(iii) In our simulation we find that Rb excited to the $5p\Pi_{3/2}$ -state remains bound to the He droplet surface where it forms a RbHe exciplex. Fig. 1 shows two deep barrierless potential wells at a Rb-He distance of about 3 \AA . In the course of the dynamics, the Rb^* atom is drawn to the well close to the droplet surface, develops a RbHe exciplex that remains bound to it, and oscillates around an equilibrium position of 3 \AA above the static equilibrium position at the dimple as shown in Fig. 6. This result is in full agreement with static QMC calculations by Leino et al.⁴⁶. However, contrary to the conjecture of that paper, in our simulations we do not find that damping of the vibrational motion of the RbHe exciplex structure leads to its desorption from the He droplet.

The dynamics of the exciplex formation process can be quantitatively represented by integrating over the He density within a spherical inclusion volume with radius r_{incl} around Rb^* . The result is shown in Fig. 7. Thus, for $r_{\text{incl}} = 5.7\text{ \AA}$, which contains the entire localized He density at the Rb^* atom without including He density of the remaining droplet, we find a rise to 75 % of the final value at $t = 20$ ps. For $t > 60$ ps the He number density stabilizes close to 1, indicating the full evolution of a RbHe exciplex containing 1 He atom. This result is in good agreement with

η (%)	v_∞ (m/s)	Kin. energy (cm^{-1})
5	bound	–
10	13.4	0.64
12.5	43.0	6.6
15	62.4	13.9
20	80.4	23.0

Table 3 Asymptotic velocity of the ejected Rb^*He exciplex for various values of the fraction η of the $5p\Pi_{3/2,1/2}$ -energy spacing of 165 cm^{-1} which is converted into kinetic energy of Rb^* by relaxation from the $5p\Pi_{3/2}$ into the $5p\Pi_{1/2}$ -state. The calculations are carried out at a delay time $\tau = 60\text{ ps}$ between photo-excitation and non-radiative de-excitation of the Rb^* atom.

the previous fs pump-probe measurements, where an increasing RbHe^+ signal was observed that reached its maximum at a delay time of about 20 ps ^{33,34}.

The finding that the RbHe exciplex remains attached to the He droplet is in apparent contradiction to experiments where the ejection of free Rb and RbHe was clearly observed^{16,31,33}. Therefore, an additional mechanism must be active that induces the desorption of the RbHe molecule off the He droplet surface.

4.2 RbHe exciplex formation around the $5p^2\Pi_{1/2}$ -state: non-radiative relaxation from the $5p^2\Pi_{3/2}$ -state

In the gas phase, a RbHe exciplex can be formed in the $5p\Pi_{1/2}$ -state if enough kinetic energy is provided by collisions such that the Rb^* can overcome the potential barrier⁵⁵. Alternatively, collisions of a RbHe formed in the $5p\Pi_{3/2}$ exciplex with another atom or complex might induce relaxation into a RbHe electronic state correlating to the Rb $5p_{1/2}$ -state. In this case the barrier is circumvented by the relaxation process, as the potential wells for the two states $\Pi_{3/2}$ and $\Pi_{1/2}$ are at similar Rb-He distances. In the condensed (droplet) phase at 0.4 K temperature, none of these mechanisms are active to explain the formation of $\text{RbHe } 5p^2\Pi_{1/2}$ exciplexes and their potential ejection.

However, Fig. 1 a) indicates another possible mechanism: Non-radiative de-excitation from the $5p\Pi_{3/2}$ to the $5p\Pi_{1/2}$ -state accompanied by transfer of energy into the relative motion of the Rb^* atom away from the He droplet. Notice from the figure that the minimum of the $5p\Pi_{3/2}$ -potential is at $\sim 12683\text{ cm}^{-1}$, and that of the $5p\Pi_{1/2}$ -potential is at $\sim 12518\text{ cm}^{-1}$; the value of this potential at the barrier is 12611 cm^{-1} . Thus, non-radiative de-excitation of the Rb^* atom may add to its original kinetic energy a fraction of this 165 cm^{-1} difference energy. Consequently, the RbHe exciplex will be ejected in the $5p\Pi_{1/2}$ -state, and not in the $5p\Pi_{3/2}$ -state that was originally photo-excited. Non-radiative electronic relaxation induced by the He droplet has been observed for a number of metal atoms^{15–18,38,41,69}. In particular, previous measurements of the dispersed fluorescence upon excitation of Rb into the $5p\Pi_{3/2}$ -state of the Rb-He droplet complex have evidenced large populations of free Rb^* atoms in the $5p\Pi_{1/2}$ -state³¹. Efficient spin-relaxation of $5p\Pi_{3/2}$ -excited Rb atoms can be rationalized by the large cross section for mixing of fine structure states in collisions of alkali metal atoms with He⁷⁰. For low-temperature Rb-He collisions, the fine structure relaxation rate

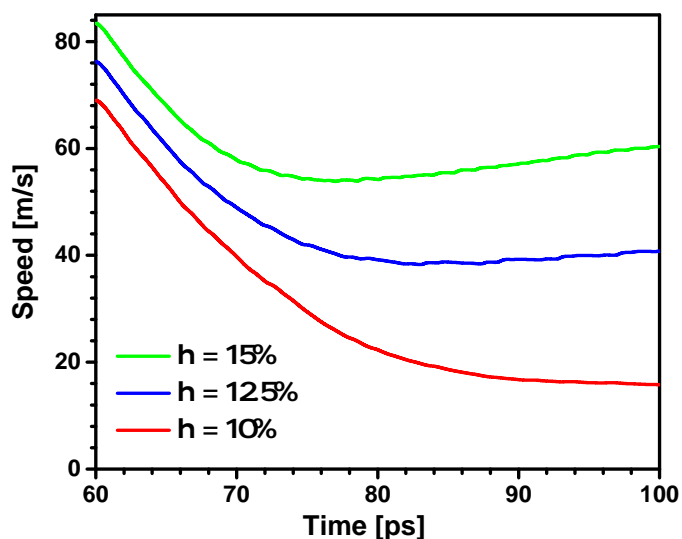


Fig. 8 (Color online) Velocity of the Rb^* atom with attached He density as a function of time after $5p\Pi_{3/2} \rightarrow 5p\Pi_{1/2}$ relaxation at $\tau = 60\text{ ps}$ for various values of the energy conversion factor η .

was found to be enhanced by the transient formation of a RbHe exciplex by orders of magnitude compared to binary Rb-He collisions⁵⁵.

Here we explore this scenario within TDDFT. Starting from Rb^* in the $5p\Pi_{3/2}$ -state, we induce a “vertical DFT transition” by suddenly switching potential energy surfaces from $5p\Pi_{3/2}$ to $5p\Pi_{1/2}$, imparting to the Rb^* a kinetic energy corresponding to a fraction η of the available non-radiative de-excitation energy. The time τ elapsing between the vertical excitation and de-excitation has to be chosen as well; this time influences the degree of $\text{RbHe } 5p\Pi_{3/2}$ exciplex formation which, as we have seen, may require some tens of ps. The actual value of these inputs cannot be determined by the model itself.

In the following, we present results obtained from simulations using as input parameters the delay before relaxation $\tau = 60\text{ ps}$, and several values of η . As shown in Fig. 6 (see also the bottom left panel of Fig. 5), this –arbitrary– time is sufficient to allow for a full development of the $5p\Pi_{3/2}$ RbHe exciplex and to bring it to a rather stationary configuration.

Fig. 5 (right column) shows snapshots of the evolution following the $5s\Sigma_{1/2} \rightarrow 5p\Pi_{3/2} \rightarrow 5p\Pi_{1/2}$ process for $\eta = 15\%$, $\tau = 60\text{ ps}$. Thus, upon sudden relaxation to the $5p\Pi_{1/2}$ -state, the Rb^*He structure promptly detaches from the remaining He droplet. The velocity of the Rb^* atom as a function of time is depicted in Fig. 8 for this and other values of η . Clearly, as the fraction of relaxation energy converted to Rb^* kinetic energy is increased from 10% to 15%, the initial speed, and even more so the asymptotic value for long evolution times rises significantly. Table 3 collects the results obtained for various values of η . It can be seen that a fairly small $\eta \geq 10\%$ is enough to induce the ejection of the Rb^*He complex. For a value $\eta = 12.5\%$, the asymptotic value of the Rb^*He velocity matches best the experimental one measured for maximum $\Pi_{3/2}$ -excitation at $\lambda = 776\text{ nm}$.

Now that we have established the Rb^*He formation and desorp-

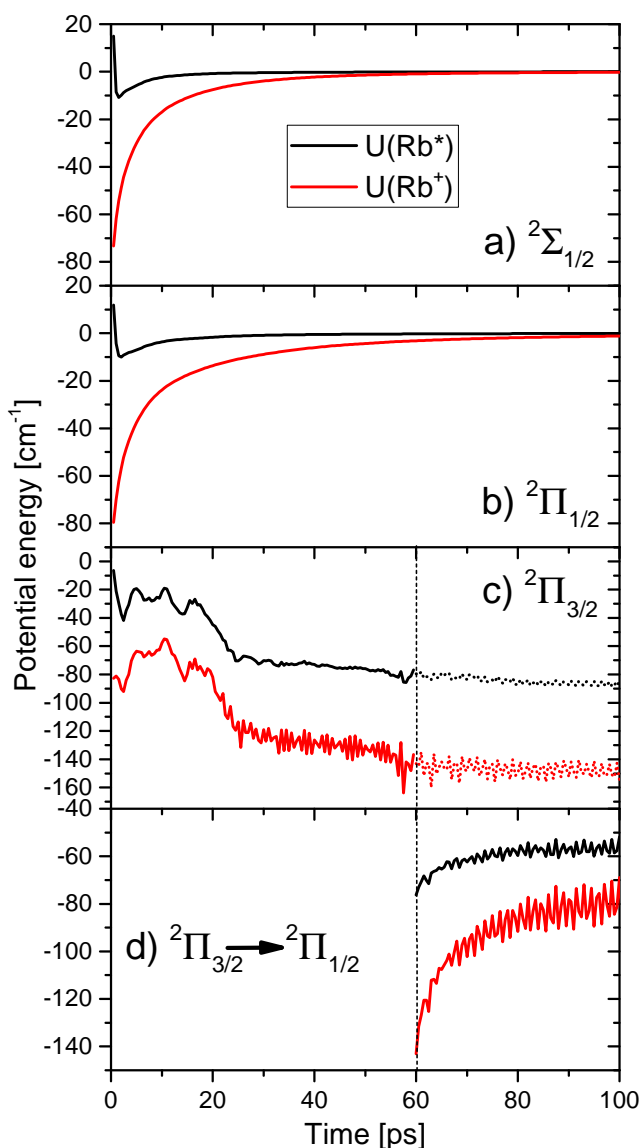


Fig. 9 (Color online) Simulated energies of the Rb-atom excited into various states interacting with the surrounding distribution of He atoms (black lines), and of the Rb⁺ ion for the same momentary geometry (red lines). In d), the excited state of Rb is suddenly switched from $\Pi_{3/2}$ to $\Pi_{1/2}$ to simulate the dynamics initiated by spin-relaxation.

tion mechanisms, we can take our comparative study one step further and compute from the simulation results the electron binding energies to compare with the experimental photoelectron spectra. For this, we evaluate the interaction energy of the Rb^{*} atom and of the Rb⁺ ion with the droplet by calculating, respectively,

$$U^*(t) = \int d\mathbf{r} \mathcal{V}_{He-Rb^*}(|\mathbf{r} - \mathbf{r}_{Rb^*}|) \rho(\mathbf{r}, t) \quad (5)$$

and

$$U^+(t) = \int d\mathbf{r} \mathcal{V}_{He-Rb^+}(|\mathbf{r} - \mathbf{r}_{Rb^+}|) \rho(\mathbf{r}, t). \quad (6)$$

Here the He-Rb⁺ pair potential is taken from Ref.³⁷.

The interaction energies $U^*(t)$ and $U^+(t)$ are shown in Fig. 9 for

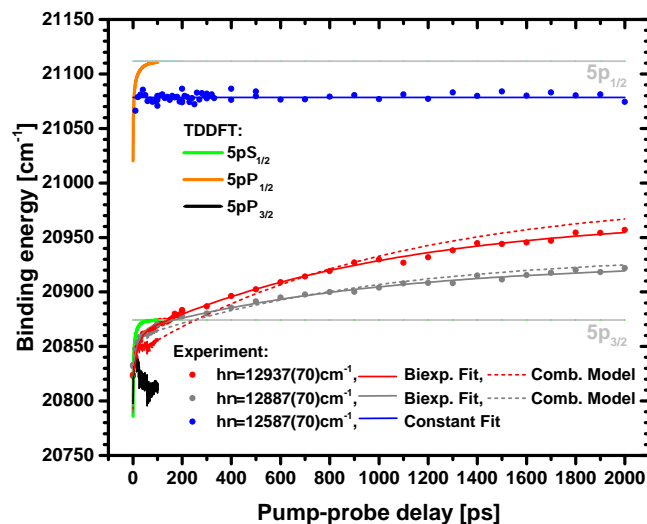


Fig. 10 Comparison of experimental and simulated electron binding energies. Thick solid lines: TD-DFT results. Dashed lines: Combined TD-DFT and analytical model. Thin solid lines: Biexponential fits of the experimental data.

Rb^{*} in the $\Sigma_{1/2}$ -state in a), in the $\Pi_{1/2}$ -state in b), and in the $\Pi_{3/2}$ -state in c). Fig. 9 d) shows the evolution following the sudden relaxation of Rb^{*} into the $\Sigma_{1/2}$ -state at $t = 60$ ps. The prompt desorption of Rb^{*} in the $\Sigma_{1/2}$ and $\Pi_{1/2}$ -states is seen as a sudden drop of $U^*(t)$ near $t = 0$ followed by a slow rise towards zero due to long-range van der Waals attraction as Rb^{*} departs from the He droplet. Due to the purely attractive interaction of the Rb⁺ ion with the He droplet, $U^+(t)$ monotonically rises to zero. The exciplex formation dynamics in the $\Pi_{3/2}$ -state is reflected by the irregular behavior of $U^*(t)$ and $U^+(t)$, eventually stabilizing at $t > 60$ ps at negative values, i.e. in a configuration where Rb^{*} is bound to the He droplet. Only when allowing for a sudden relaxation into the $\Pi_{1/2}$ -state at $t = 60$ ps, the Rb^{*}He exciplex receives a momentum “kick” and subsequently detaches from the He droplet, in spite of a rising $U^*(t)$. The asymptotic values of U^* and U^+ are then given by the binding energy of the free Rb^{*}He exciplex configuration. The fast oscillations at $t > 65$ ps indicate that Rb^{*}He keeps vibrating as it is ejected.

5 Discussion: Experiment vs. theory

Knowledge of the interaction energies $U^*(t)$ and $U^+(t)$ allows us now to determine the electron binding energy $E_b = U^+(t) - U^*(t)$ and to compare it with the experimental photoelectron spectra. Here, $U^*(t)$ and $U^+(t)$ are referenced to their asymptotic values, i.e. the binding energies of free Rb^{*} and Rb⁺, respectively. The resulting binding energies E_b are depicted as thick colored lines in Fig. 10 in the range of delay times 0-100 ps. Compared to the experimental values we note both matches and deviations. The TD-DFT value of E_b for the $\Pi_{1/2}$ -state (red line) converges within 100 ps to the value of the free Rb^{*}(5p_{1/2})-atom, as in the simulation Rb^{*} in that state detaches from the droplet. In contrast, the experimental values (blue symbols) are constant and below the atomic value because most of the atoms actually remain bound to the He droplet, see section 3.2.

The TD-DFT values for the $\Sigma_{1/2}$ -state (green line) quickly rise to $E_{5p_{3/2}}$ within a few tens of ps, again due to prompt desorption, yielding free $\text{Rb}^*5p_{3/2}$ atoms. The experimental values for excitation at 12,937 and 12,887 cm^{-1} (red and grey symbols) show a very similar increase in that time range. This supports our conclusion that the fast dynamics observed both in the photoelectron peak position and in the yield of photoions results from prompt desorption of the $\Sigma_{1/2}$ -component of the excited state.

The TD-DFT curve for the $\Pi_{3/2}$ -state without relaxation (black line) drops in binding energy, at odds with the experiment. However, when $\Pi_{3/2} \rightarrow \Pi_{1/2}$ -relaxation is included, the simulated curve also rises, staying only slightly below the experimental values in the time range 20–100 ps.

Thus, we achieve good agreement of our extended TD-DFT simulations and experiment with regard to the fast (tens of ps) desorption of the $\Sigma_{1/2}$ -state, and qualitative agreement with regard to the desorption of the $\Pi_{3/2}$ -state when allowing for spin-relaxation. The lacking quantitative agreement is not surprising given the simplicity of our assumption – instantaneous spin-relaxation. Naturally, this relaxation process has its own time dependence.

If we identify the latter with our observed slow dynamics of photoelectron spectra and ion yields, we can make up a more realistic, combined model. Hereby we account for the populations $p_{\Sigma_{1/2}}$ in the $\Sigma_{1/2}$ -state and $p_{\Pi_{3/2}}$ in the $\Pi_{3/2}$ state, which are determined by the spectral profile of the laser $I_{\ell}(h\nu)$. The coefficients $p_{\Sigma_{1/2}, \Pi_{3/2}}$ are derived from the state-selective absorption profiles $I_{\Sigma}(h\nu)$ and $I_{\Pi}(h\nu)$ using LeRoy's LEVEL program⁷¹ based on the spin-orbit corrected pseudodiatomic potentials by Callegari and Ancilotto⁶². In a second step, the absorption profiles are weighted with $I_{\ell}(h\nu)$ and integrated over $h\nu$, yielding $p(\Pi_{3/2}) = 0.28$ for the center frequency $h\nu = 12,937 \text{ cm}^{-1}$ and $p(\Pi_{3/2}) = 0.52$ for $h\nu = 12,887 \text{ cm}^{-1}$. The transient energy of the $\Pi_{3/2}$ -state, $E_{\Pi_{3/2}}(t)$, consists of a contribution $[U_{\Pi_{3/2} \rightarrow \Pi_{1/2}}^+ - U_{\Pi_{3/2} \rightarrow \Pi_{1/2}}^*]$ which relaxes to $\Pi_{1/2}$, and a contribution $[U_{\Pi_{3/2}}^+ - U_{\Pi_{3/2}}^*]$ which remains in the $\Pi_{3/2}$ -state. When assuming an exponential time dependence of the relaxation with a time constant τ , we get

$$E(t) = p_{\Sigma_{1/2}} \cdot [U_{\Sigma_{1/2}}^+ - U_{\Sigma_{1/2}}^*] + p_{\Pi_{3/2}} \cdot e^{-\ln 2 \cdot t / \tau} \cdot [U_{\Pi_{3/2}}^+ - U_{\Pi_{3/2}}^*] + p_{\Pi_{3/2}} \cdot (1 - e^{-\ln 2 \cdot t / \tau}) \cdot [U_{\Pi_{3/2} \rightarrow \Pi_{1/2}}^+ - U_{\Pi_{3/2} \rightarrow \Pi_{1/2}}^*].$$

Here, $U^*(t)$ and $U^+(t)$ are extrapolated by constants for the $\Sigma_{1/2}$ and $\Pi_{3/2}$ -states and by an exponential function for the $\Pi_{3/2} \rightarrow \Pi_{1/2}$ case for long times $t > 200$ ps. For simplicity, we neglect the 60 ps time delay between excitation and relaxation which is short compared to the full relaxation dynamics. If we assign to τ the experimental value of the slow time constant of the fit of photoelectron energies, τ^e , we obtain the dashed lines in Fig. 10, which nicely match the experimental data. This confirms our concept that the slow variations of ion and electron signals spanning hundreds of ps are due to spin-relaxation which proceeds on that time scale and causes the desorption of RbHe exciplexes, which would otherwise remain bound to the He droplet surface.

6 Conclusion

In summary, we have presented a detailed study of the formation and desorption dynamics of RbHe exciplexes initiated by laser excitation of Rb atoms attached to He nanodroplets. Experimentally, the two-color femtosecond pump-probe photoionization scheme allows us to selectively probe the dynamics of the lowest three excited states of the Rb-He droplet complex. Both photoion and photoelectron signals feature pump-probe dynamics proceeding on two distinct time scales (30 and 700 ps). By comparing with time-dependent DFT simulations, complemented by a spin-relaxation mechanism, we conclude that the fast dynamics is due to prompt desorption of Rb atoms when exciting the $\Sigma_{1/2}$ -state. The slow desorption of RbHe exciplexes is induced by $\Pi_{3/2} \rightarrow \Sigma_{1/2}$ spin-relaxation. By analyzing the rearrangement of the He surrounding the Rb atom in the $\Pi_{3/2}$ -state, we infer a formation time of the RbHe exciplex of 20 ps. When exciting the lowest state of the Rb-He droplet, $\Pi_{1/2}$, we find that a small fraction of Rb atoms desorbs as free atoms, as predicted by the DFT simulation, whereas the larger fraction Rb atoms remains bound to the He droplets.

6.0.0.1 Acknowledgements We would like to thank Marcel Drabbel for useful exchanges. Financial support by the Deutsche Forschungsgemeinschaft (MU 2347/6-1 and IRTG 2079) is gratefully acknowledged. This work has been performed under Grants No. FIS2014-52285-C2-1-P and FIS2017-87801-P from DGI, Spain, and 2014SGR401 from Generalitat de Catalunya. MB thanks the Université Fédérale Toulouse Midi-Pyrénées for financial support throughout the “Chaires d’Attractivité 2014” Programme IMDYNHE. The dynamics simulations presented in this work have been carried out thanks to the HPC resources of CALMIP supercomputing center (Grant P1039).

References

- 1 C. George, M. Ammann, B. D’Anna, D. J. Donaldson and S. A. Nizkorodov, *Chem. Rev.*, 2015, **115**, 4218–4258.
- 2 J. Schneider, D. Bahnemann, J. Ye, G. L. Puma and D. D. Dionysiou, *Photocatalysis: Fundamentals and Perspectives*, The Royal Society of Chemistry, Cambridge CB4 0WF, UK, 2016.
- 3 J. P. Toennies and A. F. Vilesov, *Angew. Chem. Int. Ed.*, 2004, **43**, 2622.
- 4 F. Stienkemeier and K. Lehmann, *J. Phys. B*, 2006, **39**, R127.
- 5 F. Ancilotto, G. DeToffol and F. Toigo, *Phys. Rev. B*, 1995, **52**, 16125–16129.
- 6 F. Stienkemeier, J. Higgins, C. Callegari, S. I. Kanorsky, W. E. Ernst and G. Scoles, *Z. Phys. D*, 1996, **38**, 253–263.
- 7 M. Barranco, R. Guardiola, S. Hernández, R. Mayol, J. Navarro and M. Pi, *J. Low Temp. Phys.*, 2006, **142**, 1–81.
- 8 C. Stark and V. V. Kresin, *Phys. Rev. B*, 2010, **81**, 085401.
- 9 L. A. der Lan, P. Bartl, C. Leidlmair, H. Schöbel, R. Jochum, S. Denifl, T. D. Märk, A. M. Ellis and P. Scheier, *J. Chem. Phys.*, 2011, **135**, 044309.
- 10 L. An der Lan, P. Bartl, C. Leidlmair, H. Schöbel, S. Denifl, T. D. Märk, A. M. Ellis and P. Scheier, *Phys. Rev. B*, 2012, **85**, 115414.

- 11 Höller, Johannes, Krotscheck, Eckhard and Zillich, Robert E., *Eur. Phys. J. D*, 2015, **69**, 198.
- 12 F. Calvo, *Phys. Rev. B*, 2017, **95**, 035429.
- 13 M. Mudrich and F. Stienkemeier, *Int. Rev. Phys. Chem.*, 2014, **33**, 301–339.
- 14 F. Ancilotto, M. Barranco, F. Coppens, J. Eloranta, N. Halberstadt, A. Hernando, D. Mateo and M. Pi, *Int. Rev. Phys. Chem.*, 2017, **36**, 621–707.
- 15 E. Loginov and M. Drabbels, *J. Phys. Chem. A*, 2007, **111**, 7504–7515.
- 16 L. Fechner, B. Grüner, A. Sieg, C. Callegari, F. Ancilotto, F. Stienkemeier and M. Mudrich, *Phys. Chem. Chem. Phys.*, 2012, **14**, 3843.
- 17 A. Kautsch, M. Koch and W. E. Ernst, *J. Phys. Chem. A*, 2013, **117**, 9621–9625.
- 18 F. Lindebner, A. Kautsch, M. Koch and W. E. Ernst, *Int. J. Mass Spectrom.*, 2014, **365–366**, 255–259.
- 19 M. Koch, G. Auböck, C. Callegari and W. E. Ernst, *Phys. Rev. Lett.*, 2009, **103**, 035302.
- 20 S. Smolarek, N. B. Brauer, W. J. Buma and M. Drabbels, *J. Am. Chem. Soc.*, 2010, **132**, 14086–14091.
- 21 A. Hernando, M. Barranco, M. Pi, E. Loginov, M. Langlet and M. Drabbels, *Phys. Chem. Chem. Phys.*, 2012, **14**, 3996–4010.
- 22 D. Mateo, A. Hernando, M. Barranco, E. Loginov, M. Drabbels and M. Pi, *Phys. Chem. Chem. Phys.*, 2013, **15**, 18388–18400.
- 23 J. von Vangerow, A. Sieg, F. Stienkemeier, M. Mudrich, A. Leal, D. Mateo, A. Hernando, M. Barranco and M. Pi, *J. Phys. Chem. A*, 2014, **118**, 6604–6614.
- 24 J. von Vangerow, O. John, F. Stienkemeier and M. Mudrich, *J. Chem. Phys.*, 2015, **143**, 034302.
- 25 A. Sieg, J. von Vangerow, F. Stienkemeier, O. Dulieu and M. Mudrich, *J. Phys. Chem. A*, 2016, **120**, 7641–7649.
- 26 J. von Vangerow, F. Coppens, A. Leal, M. Pi, M. Barranco, N. Halberstadt, F. Stienkemeier and M. Mudrich, *J. Phys. Chem. Lett.*, 2017, **8**, 307–312.
- 27 A. Przystawik, S. Göde, T. Döppner, J. Tiggesbäumker and K.-H. Meiwes-Broer, *Phys. Rev. A*, 2008, **78**, 021202.
- 28 S. Müller, S. Krapf, T. Kosłowski, M. Mudrich and F. Stienkemeier, *Phys. Rev. Lett.*, 2009, **102**, 183401.
- 29 A. Kautsch, M. Koch and W. E. Ernst, *Phys. Chem. Chem. Phys.*, 2015, **17**, 12310–12316.
- 30 J. Reho, J. Higgins, C. Callegari, K. K. Lehmann and G. Scoles, *J. Chem. Phys.*, 2000, **113**, 9694–9701.
- 31 F. R. Brühl, R. A. Trasca and W. E. Ernst, *J. Chem. Phys.*, 2001, **115**, 10220–10224.
- 32 C. P. Schulz, P. Claas and F. Stienkemeier, *Phys. Rev. Lett.*, 2001, **87**, 153401.
- 33 G. Droppelmann, O. Bünermann, C. P. Schulz and F. Stienkemeier, *Phys. Rev. Lett.*, 2004, **93**, 0233402.
- 34 M. Mudrich, G. Droppelmann, P. Claas, C. Schulz and F. Stienkemeier, *Phys. Rev. Lett.*, 2008, **100**, 023401.
- 35 S. Müller, M. Mudrich and F. Stienkemeier, *J. Chem. Phys.*, 2009, **131**, 044319.
- 36 M. Theisen, F. Lackner and W. E. Ernst, *Phys. Chem. Chem. Phys.*, 2010, **12**, 14861–14863.
- 37 A. Leal, D. Mateo, A. Hernando, M. Pi, M. Barranco, A. Ponti, F. Cargnoni and M. Drabbels, *Phys. Rev. B*, 2014, **90**, 224518.
- 38 E. Loginov, A. Hernando, J. A. Beswick, N. Halberstadt and M. Drabbels, *J. Phys. Chem. A*, 2015, **119**, 6033–6044.
- 39 M. Kuhn, M. Renzler, J. Postler, S. Ralser, S. Spieler, M. Simpson, H. Linnartz, A. G. G. M. Tielens, J. Cami, A. Mau-racher, Y. Wang, M. Alcamí, F. Martín, M. K. Beyer, R. Wester, A. Lindinger and P. Scheier, *Nat. Comm.*, 2016, **7**, 13550.
- 40 N. B. Brauer, S. Smolarek, E. Loginov, D. Mateo, A. Hernando, M. Pi, M. Barranco, W. J. Buma and M. Drabbels, *Phys. Rev. Lett.*, 2013, **111**, 153002.
- 41 M. Koch, A. Kautsch, F. Lackner and W. E. Ernst, *J. Phys. Chem. A*, 2014, **118**, 8373–8379.
- 42 Y. Seki, T. Takayanagi and M. Shiga, *Phys. Chem. Chem. Phys.*, 2017, **19**, 13798–13806.
- 43 G. Auböck, J. Nagl, C. Callegari and W. E. Ernst, *Phys. Rev. Lett.*, 2008, **101**, 035301.
- 44 M. Theisen, F. Lackner and W. E. Ernst, *J. Phys. Chem. A*, 2011, **115**, 7005–7009.
- 45 T. Takayanagi and M. Shiga, *Phys. Chem. Chem. Phys.*, 2004, **6**, 3241.
- 46 M. Leino, A. Viel and R. E. Zillich, *J. Chem. Phys.*, 2011, **134**, 024316.
- 47 C. Giese, T. Mullins, B. Grüner, M. Weidemüller, F. Stienkemeier and M. Mudrich, *J. Chem. Phys.*, 2012, **137**, 244307.
- 48 S. H. Patil, *J. Chem. Phys.*, 1991, **94**, 8089–8095.
- 49 F. Ancilotto, M. Barranco, F. Caupin, R. Mayol and M. Pi, *Phys. Rev. B*, 2005, **72**, 214522.
- 50 M. Pi, F. Ancilotto, F. Coppens, N. Halberstadt, A. Hernando, A. Leal, D. Mateo, R. Mayol and M. Barranco, *4He-DFT BCN-TLS: A Computer Package for Simulating Structural Properties and Dynamics of Doped Liquid Helium-4 Systems*. <https://github.com/bcntls2016/>, 2017.
- 51 D. Mateo, A. Hernando, M. Barranco, R. Mayol and M. Pi, *Phys. Rev. B*, 2011, **83**, 174505.
- 52 A. Hernando, M. Barranco, R. Mayol, M. Pi and M. Krośnicki, *Phys. Rev. B*, 2008, **77**, 024513.
- 53 J. Pascale, *Phys. Rev. A*, 1983, **28**, 632–644.
- 54 O. Bünermann, G. Droppelmann, A. Hernando, R. Mayol and F. Stienkemeier, 2007, **111**, 12684.
- 55 K. Hirano, K. Enomoto, M. Kumakura, Y. Takahashi and T. Yabuzaki, *Phys. Rev. A*, 2003, **68**, 012722.
- 56 A. T. J. B. Eppink and D. H. Parker, *Rev. Sci. Instrum.*, 1997, **68**, 3477.
- 57 A. Wituschek, J. von Vangerow, J. Grzesiak, F. Stienkemeier and M. Mudrich, *Rev. Sci. Instrum.*, 2016, **87**, 083105.
- 58 G. A. Garcia, L. Nahon and I. Powis, *Rev. Sci. Instrum.*, 2004, **75**, 4989–4996.
- 59 B. Dick, *Phys. Chem. Chem. Phys.*, 2014, **16**, 570–580.
- 60 A. Braun and M. Drabbels, *jcp*, 2007, **127**, 114303.
- 61 G. S. Mudholkar and A. D. Hutson, *J. Stat. Plan. Inference*, 2000, **83**, 291–309.

- 62 C. Callegari and F. Ancilotto, *J. Phys. Chem. A*, 2011, **115**, 6789–6796.
- 63 M. Theisen, F. Lackner, G. Krois and W. E. Ernst, *J. Phys. Chem. Lett.*, 2011, **2**, 2778–2782.
- 64 D. Buchta, S. R. Krishnan, N. B. Brauer, M. Drabbels, P. O’Keeffe, M. Devetta, M. Di Fraia, C. Callegari, R. Richter, M. Coreno, K. C. Prince, F. Stienkemeier, R. Moshhammer and M. Mudrich, *J. Phys. Chem. A*, 2013, **117**, 4394–4403.
- 65 E. Loginov, D. Rossi and M. Drabbels, *Phys. Rev. Lett.*, 2005, **95**, 163401.
- 66 D. S. Peterka, J. H. Kim, C. C. Wang and D. M. Neumark, *J. Phys. Chem. B*, 2006, **110**, 19945–19955.
- 67 C. C. Wang, O. Kornilov, O. Gessner, J. H. Kim, D. S. Peterka and D. M. Neumark, 2008, **112**, 9356.
- 68 M. Leino, A. Viel and R. E. Zillich, 2008, **129**, 184308.
- 69 E. Loginov and M. Drabbels, *J. Phys. Chem. A*, 2014, **118**, 2738–2748.
- 70 L. Krause, in *Adv. Chem. Phys.*, edited by J. W. McGowan (Wiley, New York), 1975.
- 71 R. LeRoy, *Chemical Physics Research Report*, University of Waterloo, CP-555, 1995, 1995.